ACS APPLIED MATERIALS & INTERFACES

Research Article

www.acsami.org

High-Performing Mesoporous Iron Oxalate Anodes for Lithium-Ion Batteries

Wei An Ang,[†,‡] Nutan Gupta,[†,§] Raghavan Prasanth,[†,‡] and Srinivasan Madhavi*[,†,‡,§]

[†]School of Materials Science and Engineering, Nanyang Technological University, 50 Nanyang Avenue, Singapore 639798, Singapore
[‡]Energy Research Institute @ NTU (ERI@N), Nanyang Technological University, 50 Nanyang Drive, Singapore 637553, Singapore
[§]TUM-CREATE Center for Electromobility, Nanyang Technological University, 62 Nanyang Drive, Singapore 637459, Singapore

Supporting Information

ABSTRACT: Mesoporous iron oxalate (FeC_2O_4) with two distinct morphologies, i.e., cocoon and rod, has been synthesized via a simple, scalable chimie douce precipitation method. The solvent plays a key role in determining the morphology and microstructure of iron oxalate, which are studied by field-emission scanning electron microscopy and high-resolution transmission electron microscopy. Crystallographic characterization of the materials has been carried out by X-ray diffraction and confirmed phase-pure $FeC_2O_4{\cdot}2H_2O$ formation. The critical dehydration process of $FeC_2O_4{\cdot}2H_2O$ resulted in anhydrous FeC_2O_4, and its thermal properties are studied by thermogravimetric analysis. The electrochemical properties of anhydrous FeC_2O_4 in Li/FeC_2O_4 cells are evaluated by cyclic voltammetry, galvanostatic charge–discharge cycling, and electrochemical impedance spectroscopy. The studies showed that the initial discharge capacities of anhydrous FeC_2O_4 cocoons and rods are 1288 and 1326 mA h g^{-1}, respectively, at 1*C* rate. Anhydrous FeC_2O_4 cocoons exhibited stable capacity even at high *C* rates (11*C*). The electrochemical performance of anhydrous FeC_2O_4 is found to be greatly influenced by the number of accessible reaction sites, morphology, and size effects.

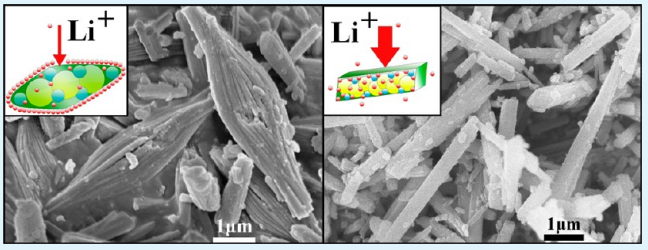

KEYWORDS: *iron oxalate, anode materials, electrode materials, lithium-ion batteries, electrochemical properties*

INTRODUCTION

Lithium (Li)-ion batteries (LIBs) are the most viable solution to a wide range of electrical energy storage applications, from portable electronics to automobiles like electric vehicles and hybrid electric vehicles to stationary applications such as telecommunication, because of their high gravimetric and volumetric energy densities.[1,2] Graphite is the widely employed anode in commercial LIBs because of it low operating voltage versus Li and acceptable rechargeability.[3,4] With the ever-increasing demand for high energy and power density LIBs, the low capacity of graphite (theoretical capacity = 372 mA h g^{-1} corresponding to LiC_6) and poor Li^+-ion intercalation kinetics have become limiting factors for practical applications. Alternative materials including silicon,[5] intermetallic alloys,[6] tin-based oxides,[7,8] and $Li_4Ti_5O_{12}$[9] have been reported as potential candidates to replace graphite. In recent years, nanostructured iron-based unitary, binary, and ternary oxides have been explored as anode materials in LIBs to improve the electrochemical properties.[10−12] In addition, transition-metal and metal nitrides, phosphides, and sulfides have also been studied in LIBs.[13,14] However, these candidates have not been able to satisfy all of the challenges in terms of performance, cost, and safety aspects of practical LIBs. Hence, efforts are underway to search for novel alternative efficient anode materials for high energy and power density LIBs.

Metal oxalates are promising anodes because of their low operating voltage (vs Li) and good reversible capacity, rate capability, and capacity retention. It is widely understood that nanomaterials with unique structures could effectively enhance the Li storage capabilities of the materials.[15] To the best of our knowledge, there are only a few reports on the effect of morphologies on the electrochemical performance of metal oxalate anodes in LIBs.[16−19] Iron oxalate[16] (FeOx) and cobalt oxalate[17] nanoribbons, prepared by a reverse-micelles process, exhibited reversible capacities of ∼700 and ∼900 mA h g^{-1} (2*C*), respectively. After 40 cycles, considerable capacity fading was observed for these metal oxalates. In view of achieving enhanced capacity and capacity retention, a mixture of transition-metal oxalates (iron–cobalt oxalate,[18] manganese–cobalt oxalate, and manganese–iron oxalate[19]) has been studied in LIBs. However, the reversible capacity of these mixed oxalates is not significantly improved.

The reverse-micelles technique is the only method thus far employed to synthesize metal oxalate anodes for LIBs.[16−19] Because of the complexity of this synthesis route, we were prompted to explore viable alternative synthesis routes for metal oxalates with improved electrochemical properties. The

Received: October 9, 2012
Accepted: November 19, 2012
Published: November 19, 2012

dx.doi.org/10.1021/am3022653 | ACS Appl. Mater. Interfaces 2012, 4, 7011−7019

uses of surfactants/capping agents, templates, catalysts, and self-assembly are key factors for anisotropic growth of materials.[20,21] As reported, surfactant-assisted synthesis techniques offer excellent control over the particle morphology, size, and distribution.[22,23] However, to control the characteristics of the particles without any use of additional ligands, an easier method using an organic solvent acting as both a reaction medium and a monodentate ligand is reported. For instance, the surfactant-free reaction of benzyl alcohol with different precursors gave rise to a whole repository of nanocrystalline metal oxides.[24,25]

This work reports a simple, surfactant-free, economical, and room temperature chimie douce technique for preparing FeOx with improved electrochemical properties as anodes for LIBs. Anhydrous FeOx (A-FeOx) with different morphologies (cocoons and rods) has been prepared and employed in a Li/FeC_2O_4 cell to study its electrochemical properties. The use of A-FeOx provides good charge−discharge properties with a stable cycling performance at high *C* rates.

EXPERIMENTAL SECTION

Synthesis of FeOx. All of the chemical reagents (analytical grade) were used as received without further purification. A total of 1 mmol of $H_2C_2O_4$ was dissolved in 10 mL of *N*,*N*-diethylacetamide (DEAc) and 10 mL of *N*-methyl-2-pyrrolidione (NMP) to obtain different morphologies. An equal molar ratio of $FeCl_2{\cdot}4H_2O$ was prepared in 5 mL of deionized water and added to the $H_2C_2O_4$ solution all at one time. The mixture was stirred for 20 min to form a homogenous solution at ambient conditions. The yellow precipitate obtained was separated by centrifugation (8000 rpm, 10 min), washed with excess ethanol, and dried under vacuum at 60 °C for 12 h (hydrated FeOx, i.e., H-FeOx). To get A-FeOx, H-FeOx samples were dried under vacuum at 185 °C for 2 h.

Material Characterization. The surface morphology and microstructures of samples were observed by field emission scanning electron microscopy (FE-SEM) using a JEOL 7600F with an accelerating voltage of 15 kV. For FE-SEM sample preparation, the samples were placed on carbon tape and sputter-coated with platinum for 40 s. Elemental compositions of samples were measured by energy-dispersive X-ray spectroscopy (EDS) using INCA mapping attached with FE-SEM. High-resolution transmission electron microscopy (HR-TEM) was performed using a JEOL 2100F microscope at an accelerating voltage of 200 kV. The samples were prepared by dispersing the powder in ethanol by ultrasonication, dropping the dispersion on a carbon-coated copper grid, and drying at ambient conditions. Crystallographic characterization was carried out by powder X-ray diffraction (XRD) using a Shimadzu XRD-6000 diffractometer operating at 40 kV and 40 mA using Cu $K\alpha_1$ radiation (λ = 0.15406 nm) with a copper target and a nickel filter. The samples were scanned between 10 and 80° (2θ) at a scan rate of 2° min^{-1}. The thermal behavior of the samples was studied by thermogravimetric analysis (TGA) using a TA Instruments Q500 analyzer at a heating rate of 5 °C min^{-1} from room temperature to 600 °C under air. The specific surface area was determined by a Brunauer−Emmett−Teller (BET) test using a Micromeritics ASAP-2020 nitrogen adsorption−desorption apparatus.

Electrochemical Measurement. The anode was prepared by mixing 60 wt % A-FeOx, 30 wt % conductive additive (Super P Li carbon, Timcal), and 10 wt % poly(vinylidene difluoride) binder (Kynar 2801) in NMP as the solvent for the binder to form the slurry. The resulting uniform slurry was cast onto etched copper foil by a doctor-blade technique followed by drying at 80 °C for 24 h under vacuum. Test cells, Li/FeC_2O_4, were fabricated in a coin cell (CR2016), and electrochemical tests were conducted using a battery test system (XWJ Neware Tech. Co., China) between 0 and 3 V at 1, 2, 3 and 11C (1C = 1 Li h^{-1} mol^{-1}, i.e., ≈0.2 mA cm^{-2}). $LiPF_6$ (1 M) in ethylene carbonate/diethyl carbonate (1:1 wt %, Danvec) was used as the electrolyte and a Celgard 2400 membrane as the separator. Cyclic voltammetry (CV) and electrochemical impedance spectroscopy (EIS) measurements were carried out on a Solartron (1470E and SI 1255B impedance/gain-phase analyzer coupled with a potentiostat) electrochemical workstation. CV was studied at 0.1 mV s^{-1} in the voltage range of 0−3 V, and EIS was studied by applying an alternating-current perturbation of 10 mV over the frequency range of 100 kHz to 5 mHz at an open-circuit potential. The Nyquist plots were analyzed using *Zplot* and *Zview* programs (version 2.2, Scribner Associates Inc., USA). All of the test cells were fabricated in an argon-filled glovebox (H_2O, O_2 < 1 ppm, Mbraun, Unilab, USA) using a Li metal foil (~0.59 mm thickness, Hohsen Corp., Japan) as counter and reference electrodes.

RESULTS AND DISCUSSION

Thermal Properties. The thermal properties of FeOx are studied by TGA. The as-synthesized H-FeOx samples (cocoons and rods, i.e., H-FeOx-C and H-FeOx-R) contained two water molecules of crystallization. From Figure 1, a weight loss of

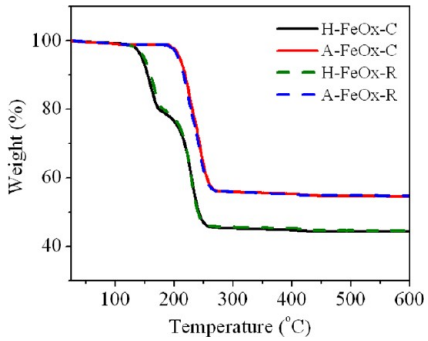

Figure 1. TGA curves (5 °C min^{-1} from room temperature to 600 °C under air).

~20 wt % is observed for H-FeOx samples at 185 °C, which is in well agreement with the theoretical weight loss according to eq 1. At 270 °C, a weight loss of ~54.5 wt % (theoretical value = 55.6 wt % according to eq 2) is observed for H-FeOx samples, which is ascribed to oxalate decomposition. After dehydration, there is no considerable weight loss observed up to 185 °C for A-FeOx samples (cocoons and rods, i.e., A-FeOx-C and A-FeOx-R). A weight loss of ~43.7 wt % (theoretical value = 44.5 wt % according to eq 3) is observed at 270 °C for A-FeOx samples. No further significant weight loss is observed above 270 °C, indicating complete decomposition of oxalate for H-FeOx and A-FeOx samples. The TGA results indicate the complete elimination of crystallized water molecules from H-FeOx at 185 °C, resulting in A-FeOx, as shown in the following equations:

Dehydration: 30 − 185 °C

$$FeC_2O_4{\cdot}2H_2O \rightarrow FeC_2O_4 + 2H_2O\uparrow \quad (1)$$

Decomposition: >185 °C

$$4FeC_2O_4{\cdot}2H_2O \rightarrow 2Fe_2O_3 + 2CO_2\uparrow + 6CO\uparrow + 8H_2O\uparrow \quad (2)$$

$$4FeC_2O_4 \rightarrow 2Fe_2O_3 + 2CO_2\uparrow + 6CO\uparrow \quad (3)$$

Structural and Morphological Characterization. H-FeOx (chemical formula $FeC_2O_4{\cdot}2H_2O$) crystallizes in two allotropic forms, α monoclinic (space group *C*2/*c*) and β orthorhombic (space group *Cccm*).[26,27] Figure 2 shows the

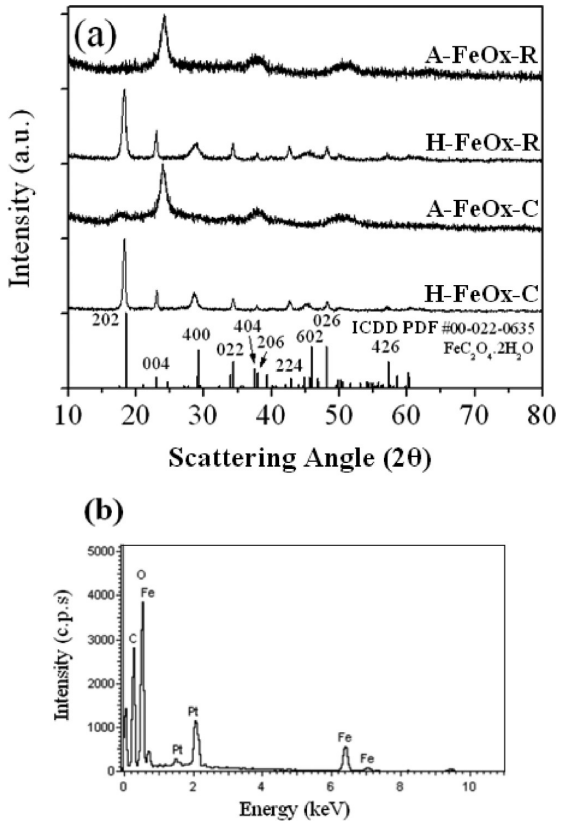

Figure 2. (a) XRD patterns for the H-FeOx and A-FeOx samples and (b) the EDS spectrum for A-FeOx-C.

XRD patterns of the H-FeOx and A-FeOx samples. All of the diffraction peaks for the H-FeOx samples are readily indexed to the orthorhombic β-phase (ICDD PDF no. 00-022-0635) with a = 12.26 Å, b = 5.57 Å, and c = 15.48 Å.[26] Compared to A-FeOx, XRD shows that the H-FeOx samples have narrow peak widths indicating larger crystallite sizes and are phase-pure materials, while the A-FeOx samples are poorly crystalline products.[16,18] Figure 2b shows the EDS spectrum of a selected A-FeOx sample, and the results are supported by XRD data. The detected platinum (Pt) was sputter-coated onto the samples prior to EDS, and no impurities were detected. To further confirm the oxidation state of iron (Fe) in the A-FeOx samples, a X-ray photoelectron spectroscopy (XPS) spectra with energy levels of Fe $2p_{3/2}$ and Fe $2p_{1/2}$ are recorded (see the Supporting Information, Figure S1). The peak positions correspond to Fe^{2+} oxidation states occurring at 709.6 and 723.6 eV,[28] indicating a phase-pure FeOx sample, which is in good agreement with the XRD studies. In addition, FT-IR spectral analysis proves the presence of an oxalate structure[17] in the A-FeOx samples (see the Supporting Information, Figure S2).

Figure 3 shows the FE-SEM micrographs of the H-FeOx and A-FeOx samples. The images show two distinct morphologies of the samples obtained depending on the solvent used. FeOx prepared in DEAc exhibited micrometer-sized cocoon-shaped particles (Figure 3a,b) with 0.7−3 μm width, 3−6 μm length, and rough surfaces. On the other hand, when NMP was used as the solvent, rectangular rods in the cross section were formed (Figure 3c,d) with relatively smooth surfaces. The rods had widths in the range of 0.3−0.5 μm and lengths in the range of submicrometer to micrometer. The rods were more densely packed compared to the cocoons. There were no considerable differences in the size and shape observed after dehydration. Furthermore, it was observed from the surface texture of A-FeOx-C that it had an onionlike-layered structure, while A-FeOx-R was probably formed by stacking of the crystal planes in the axial direction, as illustrated in Scheme 1. To further highlight the importance of the solvent in the morphological variations, the synthesis using only distilled water as the reaction medium was carried out. Irregular, shorter, and wider FeOx blocks were obtained (see the Supporting Information, Figure S3).

Fe ion and oxalic acid do not react immediately because of large differences in their ionization abilities in an organic solvent medium.[29] This may be further explained by the low

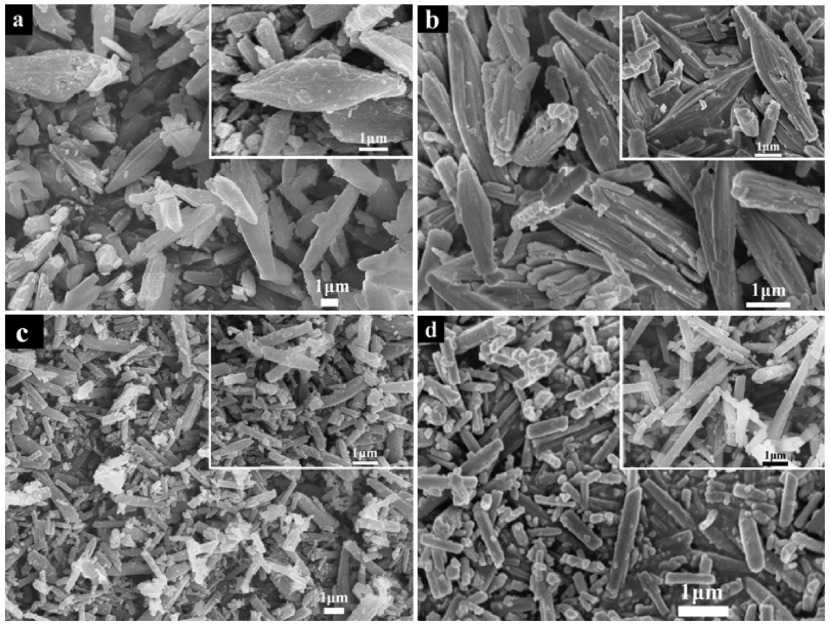

Figure 3. FE-SEM micrograph and magnified view (inset): (a) H-FeOx-C; (b) A-FeOx-C; (c) H-FeOx-R; (d) A-FeOx-R.

Scheme 1. Reaction Route for Morphological Variation

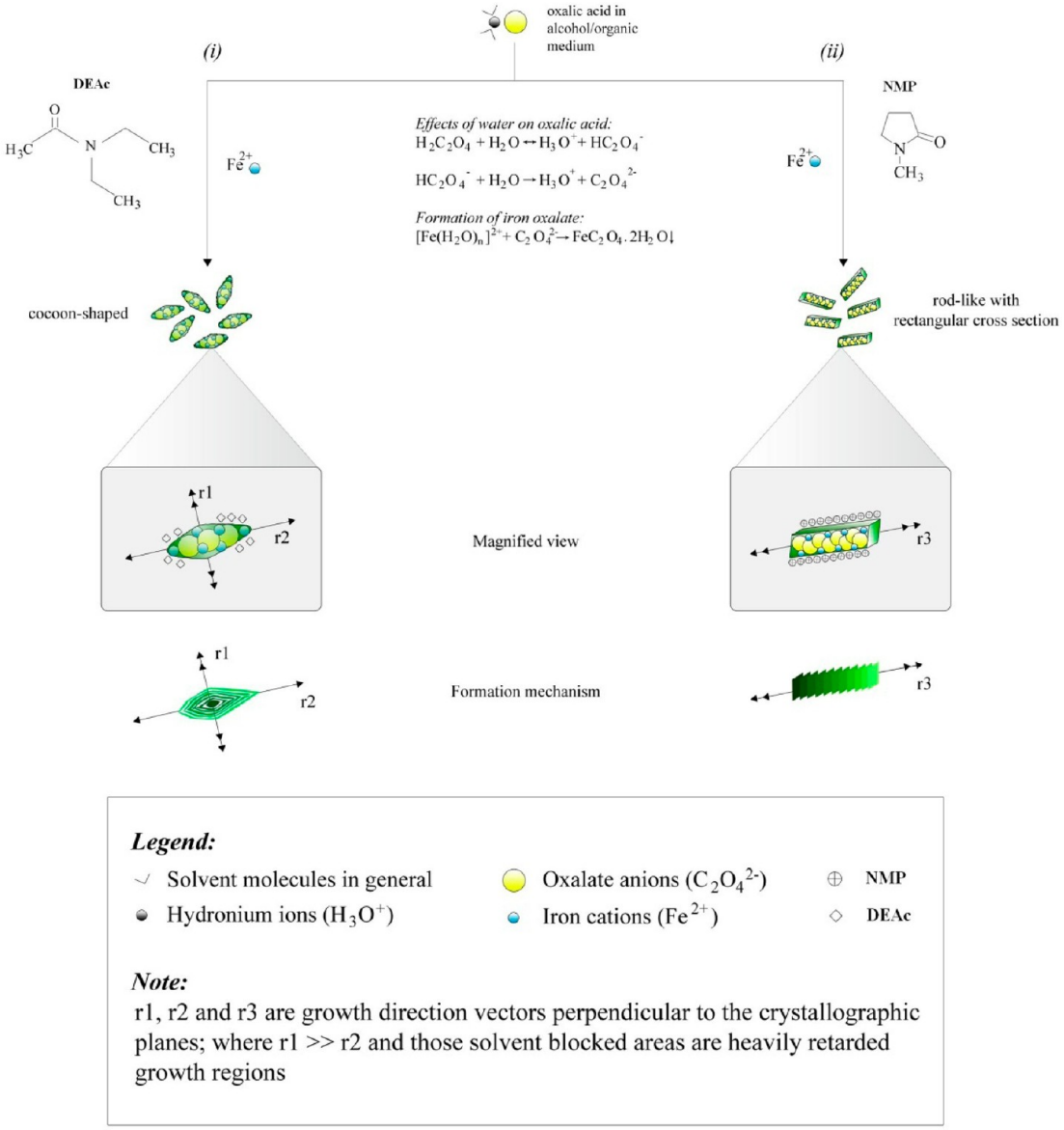

dielectric constants of DEAc (32.1) and NMP (32.5) in which weak dissociation of oxalic acid occurs compared to water (80). Previous reports show that differences in solubility, nucleation and growth of the products, reaction kinetics, solution properties, and stability of particles in different solvent systems are important factors for forming various shapes.[30] Generally, anisotropic growth of the crystal structure is a result of large differences in the surface energy between crystallographic planes.[21] This means that the selective interaction between the solvents and crystallographic planes of FeOx is the key factor in morphological variations. Hence, by controlling the ion-exchange reaction using different organic solvents, different morphologies of FeOx can be achieved. The kinetics factor and ion-exchange reaction between iron (Fe^{2+}) cations and oxalate ($C_2O_4^{2-}$) anions are different in DEAc and NMP, thus resulting in A-FeOx-C and A-FeOx-R morphologies, respectively. The variation in the molecular weights and structures of DEAc and NMP are probably some of the reasons for the differences in the kinetics factor and ion-exchange reactions. There also exist other forms of driving forces for particle structural organization that can be based on ionic, covalent, hydrogen, noncovalent, metal−ligand, and colloidal interactions.[31]

A-FeOx morphologies are further confirmed by TEM (Figure 4). The selected area electron diffraction (SAED) of A-FeOx indicates poor crystalline nature, which is in good accordance with XRD observations. From HR-TEM micrographs, it is observed that A-FeOx shows a complex porous structure. The pores can be generated from the particles as a result of the release of crystallized water molecules during the dehydration process. There are no observable lattice fringes from HR-TEM micrographs for A-FeOx, indicating a predominantly amorphous nature.

Porosity and Surface Area. To study the porosity and specific surface area of A-FeOx, BET gas sorption was carried out. The nitrogen adsorption−desorption isotherms (at 77 K) of these samples are shown in Figure 5. The samples have adsorption isotherms with the capillary condensation range starting at lower pressure and almost extending $P/P_0 = 1$, which means the samples have a high fraction of porosity.[32] The initial gases absorbed by A-FeOx-R and A-FeOx-C are 37 and 22 cm^3

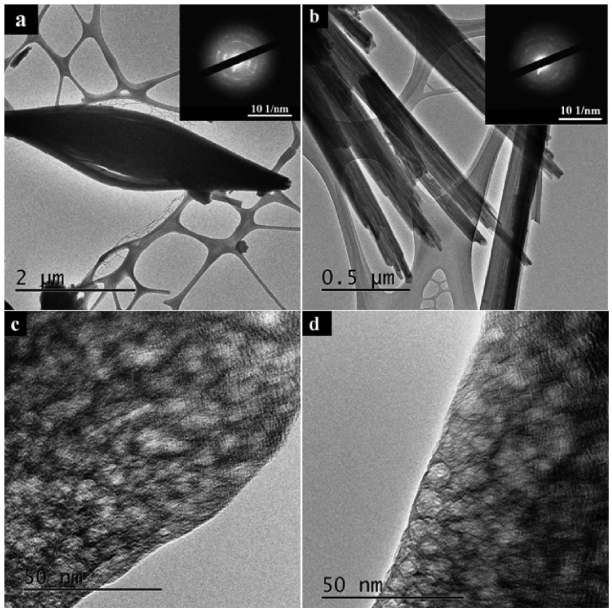

Figure 4. TEM/HR-TEM micrographs: (a and c) A-FeOx-C; (b and d) A-FeOx-R. Inset: SAED image.

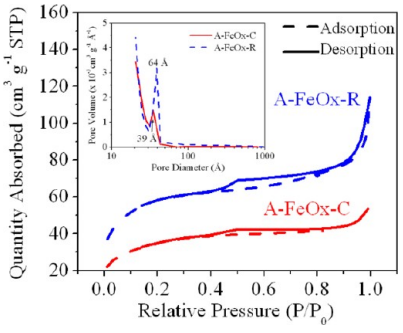

Figure 5. Nitrogen adsorption−desorption isotherm curves. Inset: BJH pore-size distribution.

g^{-1} respectively. The sharp decline in the desorption curves indicates that the samples have mesoporous structures with typical Langmuir IV type curves, while the hysteresis between adsorption and desorption from relative pressure P/P_0 = 0.4 to 0.9 demonstrates that there is a diffusion bottleneck. In the case of A-FeOx-R, when the relative pressure P/P_0 is greater than 0.9, a sudden increase appears, indicating secondary pores due to aggregation of the particles. The BET specific surface areas for A-FeOx-C and A-FeOx-R are 124 and 207 m^2 g^{-1}, respectively. As seen in Figure 5 (inset), the pore-size distribution plot obtained by the Barrett−Joyner−Halenda (BJH) method indicates that A-FeOx has a narrow pore-size distribution. The average pore diameters for A-FeOx-C and A-FeOx-R are 39 and 64 Å, respectively. BET measurements are consistent with the HR-TEM micrographs showing a mesoporous structure for A-FeOx.

CV. Electrode materials of LIBs usually exhibit electrochemical activity to react with Li$^+$ ions. In order to distinguish the electrochemical activity, CV was employed. Figure 6a shows the CV curves of A-FeOx-C electrodes cycled between 0 and 3 V at a scan rate of 0.1 mV s^{-1}. Two cathodic current peaks at 1.21 and 0.76 V were observed in the first cycle. The high-intensity peak located at 1.21 V in the first cycle shifted to higher potential (1.3 V) during the second cycle and

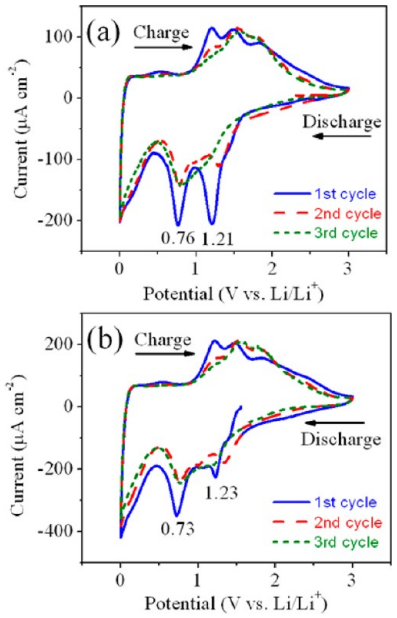

Figure 6. CV profiles at 0−3 V at a scan rate of 0.1 mV s^{-1}: (a) A-FeOx-C; (b) A-FeOx-R.

disappeared in subsequent cycles. This may be due to the following reasons: (i) decomposition of the electrolyte, which results in the formation of an organic layer deposited on the surface of the particles[33,34] and (ii) a conversion reaction of Li-ion intercalation to form $Li_2C_2O_4$ and metallic iron (Fe^0) particles, as shown in eq 4.

$$FeC_2O_4 + 2Li^+ + 2e^- \rightarrow Fe + Li_2C_2O_4 \quad (4)$$

In the anodic process, multiple stepwise oxidation of Fe is observed in the first cycle, while one broad peak (1.3−1.9 V), which corresponds to the reversible oxidation step of Fe^0 to Fe^{3+}, is seen in subsequent cycles. From Figure 6b, the CV curves for A-FeOx-R show a profile almost similar to that of A-FeOx-C but with higher current intensity peaks at 0.73 and 1.23 V. The intensity of cathodic current peak of A-FeOx-R at 0.73 V is much higher than that of 1.23 V. A peak shift from 1.23 to 1.33 V is observed during the second cycle and disappeared in subsequent cycles. It is observed that the integrated area of the cathodic/anodic peak in A-FeOx-R is almost double that of A-FeOx-C, which is associated with higher capacity and reactivity.

Evaluation in Half-Cells. Galvanostatic charge−discharge profiles of A-FeOx in Li/FeC_2O_4 test cells at 1*C* rate are shown in Figure 7a,b. It is evident from Figure 7a, during the first discharge, that the potential of the A-FeOx-C electrodes decreases sharply to 1.5 V, followed by a weak slope corresponding to the electrochemical reaction of FeC_2O_4 with Li. When the potential decreases from 0.9 to 0.74 V, a voltage plateau at ∼0.76 V is observed, indicating a reduction from Fe^{3+} to Fe^0 and thereafter followed by a smooth decrease in the voltage during discharge. It is observed that A-FeOx-C exhibits a high initial discharge capacity of 1288 mA h g^{-1}. From the 50th discharge profile, only one voltage plateau between 1 and 0.85 V corresponding to the reduction of Fe^{3+} to Fe^0 is observed. The cell delivers a discharge capacity of 869 and 825 mA h g^{-1} corresponding to the 50th and 100th cycles, respectively, with similar voltage plateaus between 1 and 0.85 V.

From Figure 7b, the potential of the A-FeOx-R electrodes decreases rapidly to about 1.46 V, and two voltage plateaus at

dx.doi.org/10.1021/am3022653 | ACS Appl. Mater. Interfaces 2012, 4, 7011−7019

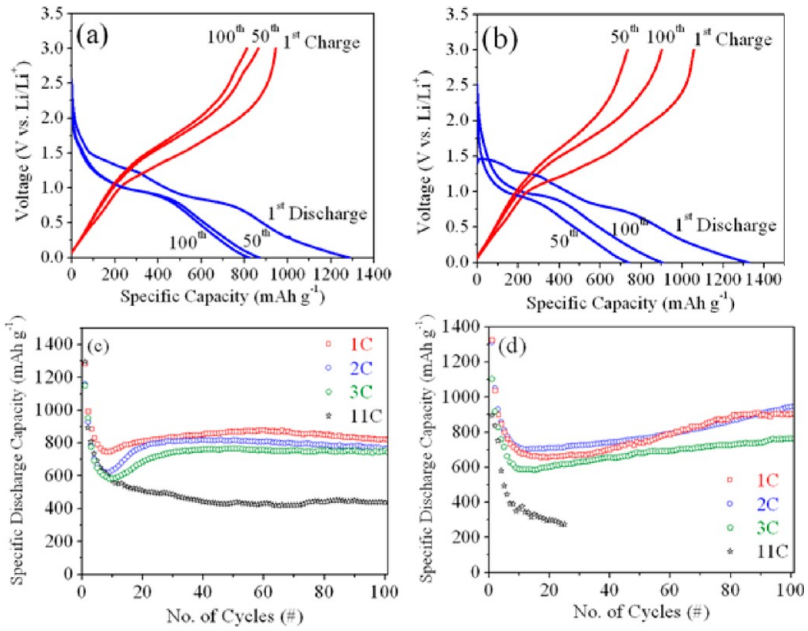

Figure 7. Charge−discharge profile versus specific capacity (1C rate) and the galvanostatic cycling performance: (a and c) A-FeOx-C; (b and d) A-FeOx-R.

Scheme 2. Li-Ion Surface and Bulk Reactions on A-FeOx Samples

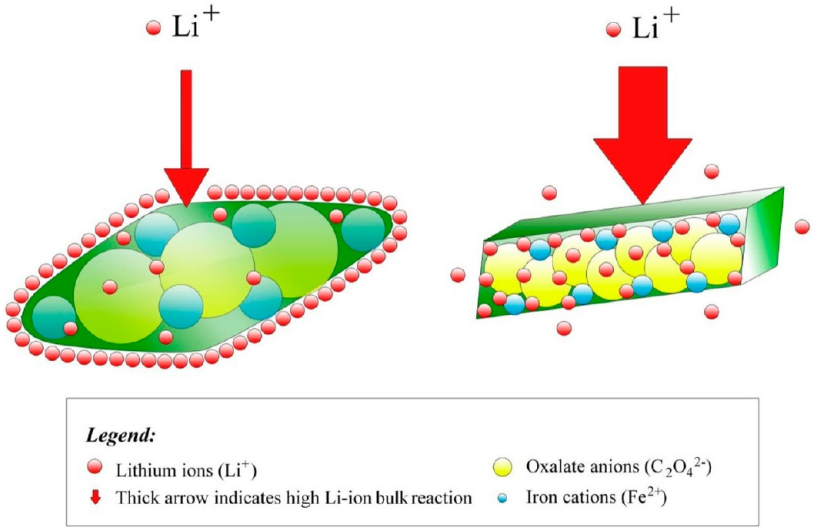

1.32 and 0.73 V with a discharge capacity of 1326 mA h g^{-1} are observed in the first discharge cycle. As in the case of A-FeOx-C, A-FeOx-R also showed only one voltage plateau around 0.9 V corresponding to a reduction from Fe^{3+} to Fe^0 observed from the 50th cycle. The discharge capacities at the 50th and 100th cycles are 739 and 906 mA h g^{-1}, respectively. Similar reasons for the electrochemical reaction of A-FeOx-C with Li occur at 1.32 V, and the reduction of Fe at 0.73 V can be attributed to A-FeOx-R. This electrochemical behavior of A-FeOx is consistent with the CV studies. The initial discharge capacity for A-FeOx is observed to be higher than the theoretical capacity of FeC_2O_4 (373 mA h g^{-1} based on eq 4), which may be due to decomposition of the nonaqueous electrolyte during discharge.[34] It is clear that the first discharge capacity is mostly due to faradaic contributions and is irreversible. The A-FeOx charge−discharge profile is observed to be significantly different from those of other conventional oxide electrodes, demonstrating that the conversion reaction may be due to lithium oxalate formation during the discharge instead of lithium oxide.[16,35]

Parts c and d of Figure 7 show the galvanostatic cycling performance of A-FeOx in Li/FeC_2O_4 test cells cycled between 0 and 3 V at different *C* rates. In the case of A-FeOx-C, it is observed that there is fast capacity fading up to 8 cycles and it starts to increase thereafter. After 25 cycles, the cells deliver stable reversible capacities of ~825, 768, 752, and 438 mA h g^{-1} at 1, 2, 3, and 11C rates, respectively, up to 100 cycles, which is 117−221% higher than the theoretical capacities. The capacity fading values after the 100th cycle for A-FeOx-C (based on the 25th cycle) are 0.2, 4, and 12% for 1, 2, and 11C rates, respectively. On the other hand, A-FeOx-R shows an initial capacity fade up to 9 cycles and starts to increase thereafter, as shown in Figure 7d. After 100 cycles, the cells deliver discharge capacities of ~906, 946, and 764 mA h g^{-1} respectively at 1, 2,

dx.doi.org/10.1021/am3022653 | ACS Appl. Mater. Interfaces 2012, 4, 7011−7019

and 3*C* rates. A coulombic efficiency of more than 98% was attained for A-FeOx at different *C* rates after 10 cycles.

It is remarkable to note that the capacity increases in A-FeOx with cycling after an initial capacity fade. This phenomenon is not yet fully understood. During cycling, the faradaic capacity is observed to be almost double that of the theoretical capacity in the proposed conversion equation (eq 4). The origin of this extra capacity is mainly due to the faradaic contribution that comes from the side reactions with the electrolyte and/or reversible formation of a gel-like layer, as reported elsewhere.[36,37] Another possible reason may be supported by the fact that the abundant pore structures cannot be fully utilized immediately during the initial cycle. A-FeOx-C showed an excellent reversible capacity of 438 mA h g^{-1} at 11*C* rate after 100 cycles, which is 118% higher than the theoretical capacity of graphite. At a higher *C* rate (11C), the cell having A-FeOx-R failed after 25 cycles. For an efficient anode material, the performance at high *C* rates is crucial for high energy and power density LIBs. Compared to other oxalates, A-FeOx prepared by the chimie douce precipitation method showed higher capacity and cycle performance even at high *C* rates.

As observed, the rate of increase in the capacity of A-FeOx-C in the first 25 cycles was faster than that of A-FeOx-R (gradual rise) at different *C* rates. This may be illustrated on the basis of Scheme 2. The phenomenon may be explained by variation in the number of accessible reaction sites, morphology, and size effects, as observed in the FE-SEM and HR-TEM micrographs of A-FeOx. The packing density of a material is one of the factors affecting electrochemical performance of the electrodes. A-FeOx-C is oval-shaped with a smaller pore size than long A-FeOx-R with flat ends. The surface texture of A-FeOx can affect the electrode/electrolyte interface and, in turn, influences the electrochemical behavior. As demonstrated in the nitrogen adsorption−desorption isotherms (Figure 5), a relative pressure P/P_0 greater than 0.9 confirms the agglomeration of A-FeOx-R, which may also affect the electrochemical performance. The observed electrochemical performance at different *C* rates may be due to the synergistic effects of the above-mentioned reasons.

The faradaic (originating from Li conversion or the insertion process and surface film formation) and nonfaradaic (double-layer effect) contributions can be separated by analyzing the CV data at different sweep rates. The area under the CV graphs represents the total amount of stored charge coming from faradaic and nonfaradiac contributions. The total current was separated into faradaic and nonfaradaic components modeled and described by Brezesinski et al.[38] for TiO_2 electrodes. A linear relationship was found between the intensities measured at different voltages by using the following equation:

$$i(\mathrm{V})\,\nu^{-0.5} = k_1\nu^{0.5} + k_2 \qquad (5)$$

where ν is the sweep rate and k_1 and k_2 are related to the current contributions from the surface capacitive and diffusion-controlled faradaic effects, respectively.

Figure 8 shows the relative current contributions of the faradaic and nonfaradic phenomena. As is clearly seen from Figure 8, the main contribution is the faradaic component for A-FeOx at different sweep rates. This indicates that at low sweep rate the reaction mechanism is dominated by Li conversion or the insertion process. However, the nonfaradaic contribution for A-FeOx increases with increasing sweep rates. A-FeOx-C presents a lower nonfaradaic contribution at low sweep rate, and the values are observed to increase from 23 to

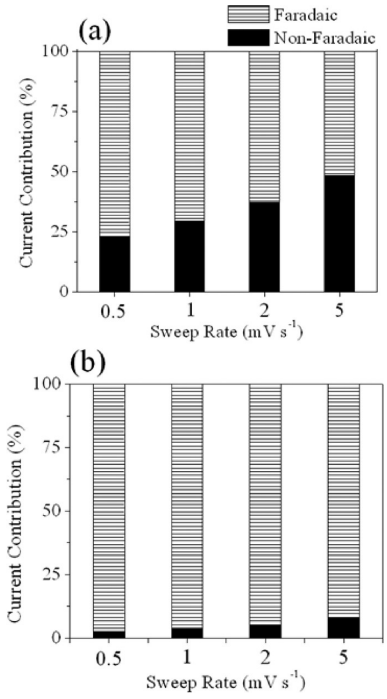

Figure 8. Relative intensities of faradaic and nonfaradaic current contributions: (a) A-FeOx-C; (b) A-FeOx-R.

48% with an increased sweep rate from 0.5 to 5 mV s^{-1}. For A-FeOx-R, the nonfaradaic contribution seems to be insignificant even at high sweep rates. These results are in agreement with the other oxalates reported.[19]

In the literature, EIS analysis on several metal oxide anodes like Co_3O_4,[39] TiO_2,[40] SnO,[41] and $Li_4Ti_5O_{12}$[42] has been analyzed and interpreted. Thus, EIS was performed on A-FeOx to understand the formation of the surface film, charge-transfer processes corresponding to Li intercalation/deintercalation, the double-layer and intercalation capacitances, and their variation with different morphologies. The rate capability and overall performance of the cell is dominated by the resistance of the films (passivation layer) formed on the surface of A-FeOx in the first lithiation step and growth of the film during subsequent charge−discharge cycling. Figure 9 displays the Nyquist plots of the EIS spectra obtained from A-FeOx in Li/FeC_2O_4 electrodes versus Li^+ at an open-circuit potential for the fresh cell (equilibrated overnight) and after 100 galvanostatic charge−discharge cycles. As shown in Figure 9a, the plots show a single semicircle in a high-to-middle (between 100 kHz to 10 Hz) frequency followed by a sloping line with a phase angle of about 45−65° to the real axis in the lower frequency range (<5 Hz), referring to the charge-transfer reaction and the diffusion of Li^+ in the active anode (A-FeOx) material, respectively. The equivalent circuit built in series or parallel combinations of electrolyte resistance (*Rs*), surface and charge-transfer (*Rsf+ct*) resistances, double-layer capacitance across the interface (*CPEsf+dl*) (constant phase element instead of pure capacitance reflects the nonhomogeneous nature of the porous composite electrode, resulting in a depressed semicircular shape),[39] Warburg impedance due to solid-state diffusion into the center of the active material particle (*Zw*), and the intercalation capacitance (*Cint*) are shown in Figure 9c. The impedance of CPE is written as follows:

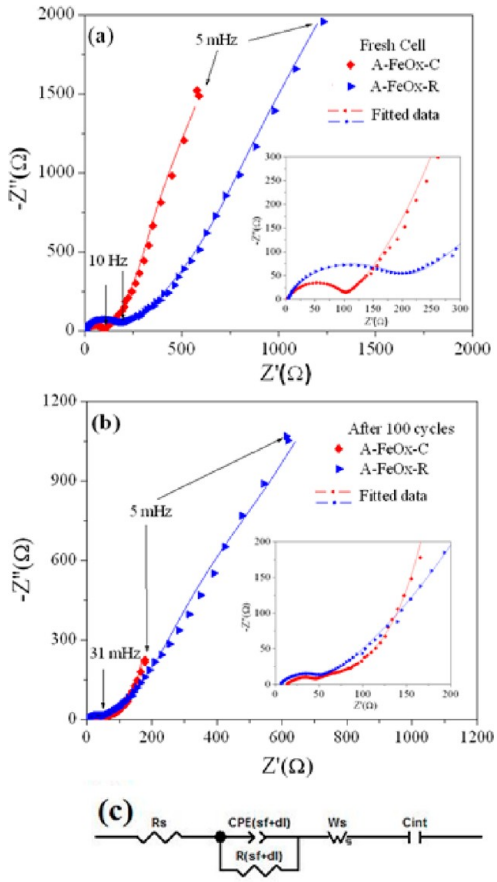

Figure 9. Nyquist plots of the A-FeOx samples: (a) fresh cells; (b) after 100 cycles; (c) equivalent circuit.

$$Z_{CPE} = 1/[Q(j\omega)^{\alpha}] \quad (6)$$

where $j = \sqrt{-1}$, ω is the angular frequency, and Q and α are constants, where $0 < \alpha < 1$. The value of α gives the degree of distortion of the impedance spectra; note that, for a value of $\alpha = 1$, Q directly corresponds to an ideal capacitor.

Table 1 displays the analysis results obtained by modelling the experimental Nyquist plots obtained for the fresh cell and after cycling, as shown in parts a and b in Figure 9, respectively. For A-FeOx-C and A-FeOx-R, the resistance values of the electrolyte and cell components (*Rs*) are observed to be 2.22 and 3.33 Ω, respectively, for the fresh cell and 10.89 and 5.87 Ω, respectively, after cycling. It is observed that A-FeOx-C has smaller charge/ion diffusion resistance (*Rsf+ct*) than A-FeOx-R at an open-circuit potential (OCV of ca. 2.7−2.9 V), reflecting that the A-FeOx-C microstructure decreases the resistance of the FeOx anode and indicating a higher number of accessible reaction sites. *Rsf+ct* of fresh cells for the A-FeOx-C and A-FeOx-R electrodes are observed to be 96.69 and 179.2 Ω, respectively, while the corresponding *CPE(sf+dl)* values are 34 and 42 μF, respectively. After cycling, the diameter of the semicircle reduces drastically followed by the well-defined Warburg region at low frequencies. This shows that *Rsf* is reduced drastically and *Rct* comes into prominence because of initiation of the intercalation/deintercalation reaction of Li into mesoporous A-FeOx. The values of the charge-transfer resistance for the A-FeOx-C and A-FeOx-R electrodes are observed to be 18.86 and 46 Ω, respectively, while the corresponding *CPE(sf+dl)* values are 227 and 202 μF, respectively. Furthermore, the α values for A-FeOx-C and A-FeOx-R are (0.74, 0.78) and (0.69, 0.60), respectively, before and after cycling. Thus, the impedance data correlated well with the galvanostatic cycling data. The intercalation capacitance *Cint* is observed to be in the range 27.9−198 mF, which is almost 3 orders of magnitude higher than the double-layer capacitance.

It is clear that the diameter of the semicircle in the A-FeOx-C electrode is significantly smaller than that of A-FeOx-R electrodes, revealing lower surface film as well as charge-transfer impedances. The A-FeOx-C structure leads to a smaller charge-transfer resistance and thus reduces the total cell resistance, which leads to a high rate capability of A-FeOx-C electrodes. This effect may be attributed to the facile charge transfer at the micrometer cocoon/electrolyte interface and also within the cocoon-like structure, owing to their porous structures and textured surfaces. The results demonstrate that A-FeOx-C electrodes exhibit excellent electrochemical performance with higher initial discharge capacity, good capacity retention, and better electrochemical activity, which may be attributed to the high surface area induced by the cocoon-like microstructure. After 100 cycles, the overall cell impedance decreases substantially compared to that of the fresh cells. This is most likely due to the unique morphology/microstructure of A-FeOx-C, where it can offer relatively higher capacity as well as improved cycling stability because of the high electrode/electrolyte interfacial area and better accommodation of volume change. As a result, the cell impedance decreases, as observed in Figure 9b. This clearly explains the reason why good rate capability is obtained for the mesoporous A-FeOx-C electrode.

CONCLUSIONS

Novel FeC_2O_4 with different morphologies, A-FeOx-C and A-FeOx-R, have been successfully synthesized by the surfactant-free chimie douce precipitation method and investigated as potential negative electrodes in LIBs. Material morphologies in the aforementioned soft chemistry process can be achieved by controlling the nucleation and growth processes. FE-SEM and HR-TEM characterizations showed that A-FeOx-C exhibited a relatively rough surface compared to A-FeOx-R. A-FeOx-C and A-FeOx-R are micrometer-sized and mesoporous in structure with high surface area. The cell with A-FeOx-C and A-FeOx-R showed properties superior to those reported for FeOx's and delivered initial discharge capacities of 1288 and 1326 mA h

Table 1. Fitting Parameters of the Cell with A-FeOx Electrodes for the Fresh Cell Equilibrated Overnight and after 100 Charge−Discharge Cycles at an Open-Circuit Potential

active material	cell configuration (tested)	*Rs* (Ω)	*R(sf+ct)* (Ω)	*CPE(sf+dl)* (μF)	α	*Zw* (Ω)	*Cint* (mF)
A-FeOx-C	fresh cell	2.22	96.69	34	0.74	1052	31.9
	after 100 cycles	10.89	18.86	227	0.69	1893	198
A-FeOx-R	fresh cell	3.33	179.2	42	0.78	2500	27.9
	after 100 cycles	5.87	46	202	0.60	924	45.2

g^{-1}, respectively. Compared to A-FeOx-R, the cell with A-FeOx-C outperformed and exhibited an excellent reversible capacity of 438 mA h g^{-1} at 11C rate and stable cycling properties. Moreover, the economical, room temperature, surfactant-free, and scalable chimie douce synthesis of materials makes them a viable option to prepare materials with controlled morphologies.

■ ASSOCIATED CONTENT

Ⓢ Supporting Information

FE-SEM micrograph and XPS and FT-IR spectra. This material is available free of charge via the Internet at http://pubs.acs.org.

■ AUTHOR INFORMATION

Corresponding Author

*E-mail: madhavi@ntu.edu.sg. Tel: +65 67904606. Fax: +65 67909081.

Notes

The authors declare no competing financial interest.

■ ACKNOWLEDGMENTS

The authors are thankful for support through funding from the National Research Foundation, Clean Energy Research Project (Grant NRF2009EWT-CERP001-036). The electron microscopy and XRD experiments were performed at the Facility for Analysis, Characterization, Testing and Simulation (FACTS) in Nanyang Technological University, Singapore.

■ REFERENCES

(1) Armand, M.; Tarascon, J. M. *Nature* **2008**, *414*, 652.
(2) Etacheri, V.; Marom, R.; Elazari, R.; Salitra, G.; Aurbach, D. *Energy Environ. Sci.* **2012**, *4*, 3243.
(3) Sawai, K.; Iwakoshi, Y.; Ohzuku, T. *Solid State Ionics* **1994**, *69*, 273.
(4) Mabuchi, A.; Tokumitsu, K.; Fujimoto, H.; Kasuh, T. *J. Electrochem. Soc.* **1995**, *142*, 1041.
(5) Chou, S. L.; Wang, J. Z.; Choucair, M.; Liu, H. K.; Stride, J. A.; Dou, S. X. *Electrochem. Commun.* **2010**, *12*, 303.
(6) Larcher, D.; Beaulieu, L. Y.; MacNeil, D. D.; Dahn, J. R. *J. Electrochem. Soc.* **2000**, *147*, 1658.
(7) Valvo, M.; Lafont, U.; Simonin, L.; Kelder, E. M. *J. Power Sources* **2007**, *174*, 428.
(8) Li, H.; Huang, X.; Chen, L. *Solid State Ionics* **1999**, *123*, 189.
(9) He, N.; Wang, B.; Huang, J. *J. Solid State Electrochem.* **2010**, *14*, 1241.
(10) Chen, J. S.; Zhu, T.; Yang, X. H.; Yang, H. G.; Lou, X. W. *J. Am. Chem. Soc.* **2010**, *132*, 13162.
(11) Chen, X.; Unruh, K. M.; Ni, C. Y.; Ali, B.; Sun, Z. C.; Lu, G. Q.; Deitzel, J.; Xiao, J. Q. *J. Phys. Chem. C* **2011**, *115*, 373.
(12) NuLi, Y. N.; Qin, Q. Z. *J. Power Sources* **2005**, *142*, 292.
(13) Nazri, G. A.; Pistoia, G. *Lithium Batteries—Science and Technology*; Kluwer Academic: New York, 2003.
(14) Grugeon, S.; Laruelle, S.; Dupont, L.; Tarascon, J. M. *Solid State Sci.* **2003**, *5*, 895.
(15) Wu, H. B.; Chen, J. S.; Hng, H. H.; Lou, X. W. *Nanoscale* **2012**, *4*, 2526.
(16) Aragon, M. J.; Leon, B.; Perez-Vicente, C.; Tirado, J. L. *Inorg. Chem.* **2008**, *47*, 10366.
(17) Aragon, M. J.; Leon, B.; Perez-Vicente, C.; Tirado, J. L.; Chadwick, A. V.; Berko, A.; Beh, S. Y. *Chem. Mater.* **2009**, *21*, 1834.
(18) Aragon, M. J.; Leon, B.; Serrano, T.; Perez-Vicente, C.; Tirado, J. L. *J. Mater. Chem.* **2011**, *21*, 10102.
(19) Leon, B.; Perez-Vicente, C.; Tirado, J. L. *Solid State Ionics* **2012**, DOI: 10.1016/j.ssi.2011.12.012.
(20) Wang, X.; Li, Y. D. *Inorg. Chem.* **2006**, *45*, 7522.
(21) Jun, Y. W.; Choi, J. S.; Cheon, J. *Angew. Chem., Int. Ed.* **2006**, *45*, 3414.
(22) Scher, E. C.; Manna, L.; Alivisatos, A. P. *Philos. Trans. R. Soc. London* **2003**, *A 361*, 241.
(23) De Mello Donega, C.; Liljeroth, P.; Vanmaekelbergh, D. *Small* **2005**, *1*, 1152.
(24) Niederberger, M.; Garnweitner, G.; Buha, J.; Polleux, J.; Ba, J.; Pinna, N. *J. Sol−Gel Sci. Technol.* **2006**, *40*, 259.
(25) Garnweitner, G.; Niederberger, M. *J. Am. Ceram. Soc.* **2006**, *89*, 1801.
(26) Deyrieux, R.; Peneloux, A. *Bull. Soc. Chim. Fr.* **1969**, *8*, 2675.
(27) Sledzinska, I.; Murasik, A.; Piotrowski, M. *Physica* **1986**, *138B*, 315.
(28) Lu, S.; Qin, W.; Wu, X.; Wang, X.; Zhao, G. *Mater. Chem. Phys.* **2012**, *135*, 58.
(29) Fuoss, R. M. *J. Am. Chem. Soc.* **1958**, *80*, 5059.
(30) Polleux, J.; Antonietti, M.; Niederberger, M. *J. Mater. Chem.* **2006**, *16*, 3969.
(31) Ozin, G. A. *Chem. Commun.* **2000**, 419.
(32) Antonelli, D. M.; Ying, J. Y. *Angew. Chem., Int. Ed.* **1995**, *34*, 2014.
(33) Larcher, D.; Bonnin, D.; Cortes, R.; Rivals, I.; Personnaz, L.; Tarascon, J. M. *J. Electrochem. Soc.* **2003**, *150*, A1643.
(34) Chen, J.; Xu, L. N.; Li, W. Y.; Gou, X. L. *Adv. Mater.* **2005**, *17*, 582.
(35) Reddy, M. V.; Yu, T.; Sow, C.-H.; Shen, Z. X.; Lim, C. T.; Subba Rao, G. V.; Chowdari, B. V. R. *Adv. Funct. Mater.* **2007**, *17*, 2792.
(36) Hassan, M. F.; Rahman, M. M.; Guo, Z. P.; Chen, Z. X.; Liu, H. K. *Electrochim. Acta* **2010**, *55*, 5006.
(37) Poizot, P.; Laurelle, S.; Grugeon, S.; Tarascon, J. M. *J. Electrochem. Soc.* **2002**, *149*, A1212.
(38) Brezesinski, T.; Wang, J.; Polleux, J.; Dunn, B.; Tolbert, S. H. *J. Am. Chem. Soc.* **2009**, *131*, 1802.
(39) Kang, J. G.; Ko, Y. D.; Park, J. G.; Kim, D. W. *Nanoscale Res. Lett.* **2008**, *3*, 390.
(40) Wang, J.; Zhou, Y.; Hu, Y.; O'Hayre, R.; Shao, Z. *J. Phys. Chem. C* **2011**, *115*, 2529.
(41) Li, H.; Huang, X.; Chen, L. *J. Power Sources* **1999**, *81-82*, 340.
(42) Wang, G. X.; Bradhurst, D. H.; Dou, S. X.; Liu, H. K. *J. Power Sources* **1999**, *83*, 156.